


5-2016

# Optical Analysis and Fabrication of Micro and Nanoscale Plasmonically Enhanced Devices

Avery M. Hill

*University of Arkansas, Fayetteville*

Follow this and additional works at: <http://scholarworks.uark.edu/meeguht>

 Part of the [Computational Engineering Commons](#), [Computer-Aided Engineering and Design Commons](#), [Engineering Physics Commons](#), [Nanoscience and Nanotechnology Commons](#), and the [Optics Commons](#)

---

## Recommended Citation

Hill, Avery M., "Optical Analysis and Fabrication of Micro and Nanoscale Plasmonically Enhanced Devices" (2016). *Mechanical Engineering Undergraduate Honors Theses*. 52.  
<http://scholarworks.uark.edu/meeguht/52>

This Thesis is brought to you for free and open access by the Mechanical Engineering at ScholarWorks@UARK. It has been accepted for inclusion in Mechanical Engineering Undergraduate Honors Theses by an authorized administrator of ScholarWorks@UARK. For more information, please contact [scholar@uark.edu](mailto:scholar@uark.edu), [ccmiddle@uark.edu](mailto:ccmiddle@uark.edu).

# **Optical Analysis and Fabrication of Micro and Nanoscale Plasmonically Enhanced Devices**

An Honors Thesis submitted in partial fulfillment of the requirements  
for Honors Studies in Mechanical Engineering

By

Avery Hill

Spring 2016  
Mechanical Engineering  
College of Engineering  
**The University of Arkansas**

Optical Analysis and Fabrication of Micro and Nanoscale Plasmonically Enhanced Devices

A thesis submitted in partial fulfillment  
of the requirements for the degree of  
Mechanical Engineering

by

Avery Hill

May 2016  
University of Arkansas



---

Dr. Paul Millet  
Thesis Director



---

Dr. Rick Couvillion  
Committee Member

# Table of Contents

<b>Acknowledgements</b> .....	<b>3</b>
<b>Collaborators</b> .....	<b>4</b>
<b>Abstract</b> .....	<b>5</b>
<b>List of Figures</b> .....	<b>6</b>
<b>Chapter 1: Introduction</b> .....	<b>8</b>
<b>1.1 Plasmons</b> .....	<b>8</b>
<b>1.2 Plasmonic Applications</b> .....	<b>9</b>
<b>1.3 Plasmonic Polarization</b> .....	<b>10</b>
<b>1.4 Computational Electromagnetics</b> .....	<b>11</b>
<b>1.5 Thesis Motivation</b> .....	<b>16</b>
<b>Chapter 2: Interdigital Photodetectors</b> .....	<b>17</b>
<b>2.1 Device Architecture and Simulation Setup</b> .....	<b>17</b>
<b>2.2 FEM Analysis</b> .....	<b>19</b>
<b>2.3 Electrode Gap Dependence</b> .....	<b>20</b>
2.3.1 Micro-gaps.....	20
2.3.1 Nano-gaps.....	23
<b>2.4 Polarization Dependence</b> .....	<b>24</b>
<b>Chapter 3: Au Thin-Film Microstructure</b> .....	<b>27</b>
<b>3.1 Device Architecture and Simulation Setup</b> .....	<b>27</b>
<b>3.2 Experimental Photocurrent Generation and Calculated Optical Enhancement</b> .....	<b>29</b>
<b>3.3 Improvement Factors</b> .....	<b>30</b>
<b>3.4 FEM Optical Enhancement Distribution</b> .....	<b>31</b>
<b>Chapter 4: Conclusion</b> .....	<b>34</b>
<b>Bibliography</b> .....	<b>36</b>

## Acknowledgements

I would like to thank Dr. Joseph Herzog for taking a chance on a sophomore with no research experience and inviting me to join his research group. I would also like to thank Ahmad Nusir for fabricating and performing all experimental tests for the devices in this work and the concurrent support he received from Dr. Omar Manasreh. I would like to thank Dr. Woodrow Shew, Dr. Paul Millet, and Dr. Joseph Herzog for serving on my honors thesis committee.

I would also like to thank Ahmad Nusir for fabricating the electrode devices in this work as well as experimentally testing all of the devices. I would also like to thank Stephen Bauman for his help with fabricating other nanodevices that contributed to other works. I would like to thank Jonathan Mishler, Cameron Saylor, Eric Novak, Paul Nguyen, and Grant Abbey for aiding the simulation process and for meaningful conversations about COMSOL.

I would also like to thank my wife, for putting up with the many hours that I spent conducting research, compiling data and figures, and putting this paper and presentation together. P.s. I did not cure cancer.

Note: This work has been submitted and published in [8] and [10] and another is in progress [23]. Other computational work completed by A. Hill was submitted and published in [26].

## Collaborators

### **Plasmonic Nano-Optics Lab Members:**

- Avery Hill (undergrad)
- Grant Abbey (REU Student 2015)
- Stephen Bauman (MicroEP Grad Student)
- **PI:** Dr. Herzog

### **Optoelectronics Research Lab Members:**

- Ahmad Nusir (EE Grad Student)
- **PI:** Dr. Manasreh

## Abstract

Plasmonic nanostructures have been shown to act as optical antennas that enhance optical devices due to their ability to focus light below the diffraction limit of light and enhance the intensity of the incident light. This study focuses on computational electromagnetic (CEM) analysis of two devices: 1) GaAs photodetectors with Au interdigital electrodes and 2) Au thin-film microstructures. Experiments showed that the photoresponse of the interdigital photodetectors depend greatly on the electrode gap and the polarization of the incident light. Smaller electrode gap and transverse polarization give rise to a larger photoresponse. It was also shown that the response from the introduction of the Au thin-film microstructure in the electrode structure was greater. The experimental device enhancement found for the introduction of the thin-film microstructures is most likely attributed to hot electron excitation. This computational study will simulate the optical properties of these two devices in order to determine what plasmonic properties and optical enhancement these devices may have. The modeling software used to validate the experimental results solved Maxwell's equations with a finite element method (FEM) mathematical algorithm provided by COMSOL Multiphysics. For the interdigital photodetectors device, it was determined that the device response as a function of electrode gap and incident light polarization angle were similar to the experimental results. The enhancement provided by the introduction of the Au thin-film microstructures cannot be completely explained by plasmonic activity occurring with the microstructures, but there is plasmonic activity occurring with the devices.

## List of Figures

**Figure 1:** (a) Metallic structures at rest with no applied electromagnetic fields. (b) Metallic structures with applied electromagnetic field with shown polarization and poynting vector, eliciting charge oscillations along the surface of the metallic structures with positive/negative localizations shown.

**Figure 2:** Application of plasmonic effects for (a) improved photovoltaic cells, (b) plasmonic lasers: SPASERs, and (c) photothermal therapies

**Figure 3:** Computational electromagnetic modeling results showing plasmonic polarization dependence for both (a) and (c) transverse and (b) and (d) longitudinal polarizations. Plasmonic polarization dependence is shown for both (a-b) rectangular and (c-d) circular shapes.

**Figure 4:** Finite Element Method (FEM) discretization of sample simulation space. Free triangular meshing pattern, simplifies complex partial differential equations that describe electromagnetic wave propagation into simple polynomials for each mesh element.

**Figure 5:** (a) Two dimensional rendering of sample structure, two-dimensional structures are treated as infinitely long in longitudinal direction, (b) SolidWorks model of the two dimensional structure with infinitely long geometry in the z-direction (longitudinal).

**Figure 6:** FEM result for sample structure shows optical enhancement distribution results for the sample structure and the direction of electromagnetic wave propagation and polarization.

**Figure 7:** Microscopic views of the interdigital photodetectors of both (a) aerial, top-down and (b) cross-sectional slices of interdigital “fingers” with electrode width  $w$  and electrode gap  $g$ .

**Figure 8:** Simulation space creation for the interdigital photodetectors complete with: all material types (Au, Ti, GaAs), geometric conditions (electrode width and gap), electromagnetic wave polarization and poynting vector, periodic boundary conditions on the left and right boundaries, and perfectly matched layers on the top and bottom boundaries

**Figure 9:** FEM result for structure shown in Figure 8 shows optical enhancement distribution results for the interdigital photodetector and the direction of electromagnetic wave propagation. Area encompassed by the dashed box is the GaAs substrate that is integrated over in order to determine the Optical Enhancement in the GaAs.

**Figure 10:** Electrode gap experimental results of interdigital photodetectors shown in Figure 7 showing (a) band gap of GaAs at 875 nm and increase in spectral response as electrode gap is reduced and (b) normalized spectral response at 875 nm wavelength band gap of GaAs. (c) Normalized computational results of the interdigital photodetectors simulation space shown in Figure 8.



**Figure 11:** Optical enhancements of Au nanostructure showed in (i) with gap spacing,  $g$ , variable from 1 nm to 50 nm. (i) Au Nanostructure with constant  $t_{Au}$  and variable gap spacing  $g$ .

**Figure 12:** Optical enhancement of interdigital photodetector configuration shown in (i). Optical enhancement is a function of electrode gap, which impacts the electrode width, and periodicity of the device architecture.

**Figure 13:** (a) and (b) Polarization study of the interdigital photodetectors with electrode gap 5  $\mu\text{m}$  showing (a) spectral study of the photodetector with peak response at 875 nm wavelength and (b) measured spectral response shown by the green squares and calculated photocurrent generation by the computation electromagnetic studies shown by the blue circles; both measured SR and calculated IP are shown for different incident electromagnetic wave polarizations.

**Figure 14:** Microscopic views of Au thin-film microstructure device of both (a) aerial, top-down and (b) linear array structures with 100 micron transverse separation, 40 micron longitudinal separation, and 20 micron structure length.

**Figure 15:** Simulation space creation for the thin-film microstructure device complete with: all material types (Au, Ti, GaAs), geometric conditions (slab width and spacing and Au and Ti thicknesses), electromagnetic wave polarization and poynting vector, periodic boundary conditions on the left and right boundaries, and perfectly matched layers on the top and bottom boundaries

**Figure 16:** (a) and (b) experimental results show improvement in photocurrent generation of microstructure devices for (a) no Ti adhesion layer and variable Au thickness and (b) constant 10 nm Au thickness and variable Ti thickness. (c) and (d) computation results showing optical enhancement measured in the GaAs substrate for (c) no Ti adhesion layer and variable Au thickness and (d) constant 10 nm Au thickness and variable Ti thickness.

**Figure 17:** Improvement in (a) and (b) spectral response and in (c) and (d) optical enhancement. Where (a) and (c) have no Ti adhesion layer and variable Au thickness and (b) and (d) have constant 10 nm Au thickness and variable Ti thickness. Computation results in (c) and (d) showing improvement in optical enhancement as negative is indicative of no plasmonic improvement from the introduction of the microstructure in the device architecture.

**Figure 18:** Optical enhancement distributions for microstructure devices (a), (b), and (c) variable Au thicknesses and no Ti adhesion layer and for (d), (e), and (f) variable Ti thickness and a constant 10 nm Au thickness

# Chapter 1: Introduction

## 1.1 Plasmons

Plasmonics is the study of the interaction between free electrons along the surface of metallic structures and the metallic structures themselves. These plasmons are collective electron charge densities that oscillate along the surface of the metallic structure.<sup>1</sup> Plasmons and plasmonics have grown tremendously as a field of study because of the ability of these plasmons to focus light at scales smaller than the diffraction limit.<sup>2</sup> These plasmonic effects provide unique optical characteristics shown by plasmonic devices and structures. The structures act as optical antennae that enhance optical emission and reception. One of the main advantages to employing these plasmonic structures is their ability to interact with and enhance electromagnetic waves at the nanoscale. Improvements in nanotechnology have allowed the proliferation of plasmonic study and enabled a wide array of researchers to study the nanoscale interaction of light.<sup>3</sup>

A metallic nanostructure with no applied electromagnetic field can be roughly modeled as an electrically neutral structure with protons and electrons balanced as shown in Figure 1(a). The plasmonic effects can be analyzed classically using Maxwell's equations governing electrodynamics.<sup>4</sup> The effect of an applied electromagnetic wave incident on a metallic structure is shown in Figure 1.

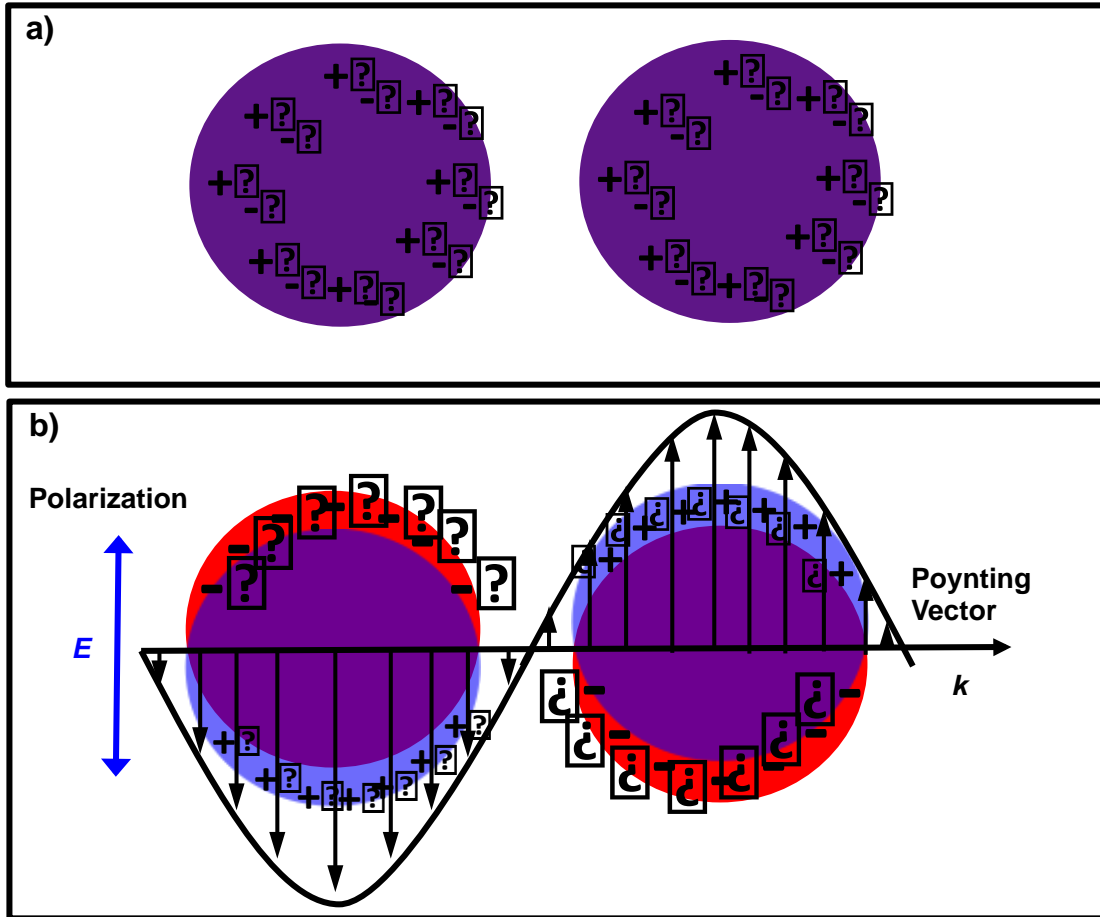


**Figure 1:** (a) Metallic nanostructures at rest with no applied electromagnetic fields. (b) Metallic nanostructures with applied electromagnetic field with shown polarization and poynting vector, eliciting charge oscillations along the surface of the metallic structures with positive/negative localizations shown.

Two metallic nano-spheres shown in Fig. 1(a) have a balanced atomic structure without any incident electromagnetic waves. Fig. 1 (b) displays the effect of an applied electromagnetic wave with shown polarization and direction of wave propagation. The applied wave causes a displacement in the electrons creating negative ions (red spheres in image) and leaving positive ions behind (blue spheres).

## 1.2 Plasmonic Applications

The usefulness of plasmonic effects is attributed to their ability to focus light at the nanoscale, below the diffraction limit of light and enhance the optical emission and

reception. This leads to applications in enhanced spectroscopies<sup>5-7</sup>, enhanced photodetectors<sup>8-10</sup>, thermoplasmonic applications<sup>11-13</sup>, improved photovoltaics<sup>14-15</sup>, photothermal therapies<sup>16</sup>, plasmonic lasers, SPASERS<sup>17</sup>, and many more. A summary of these applications is found in Figure 2.

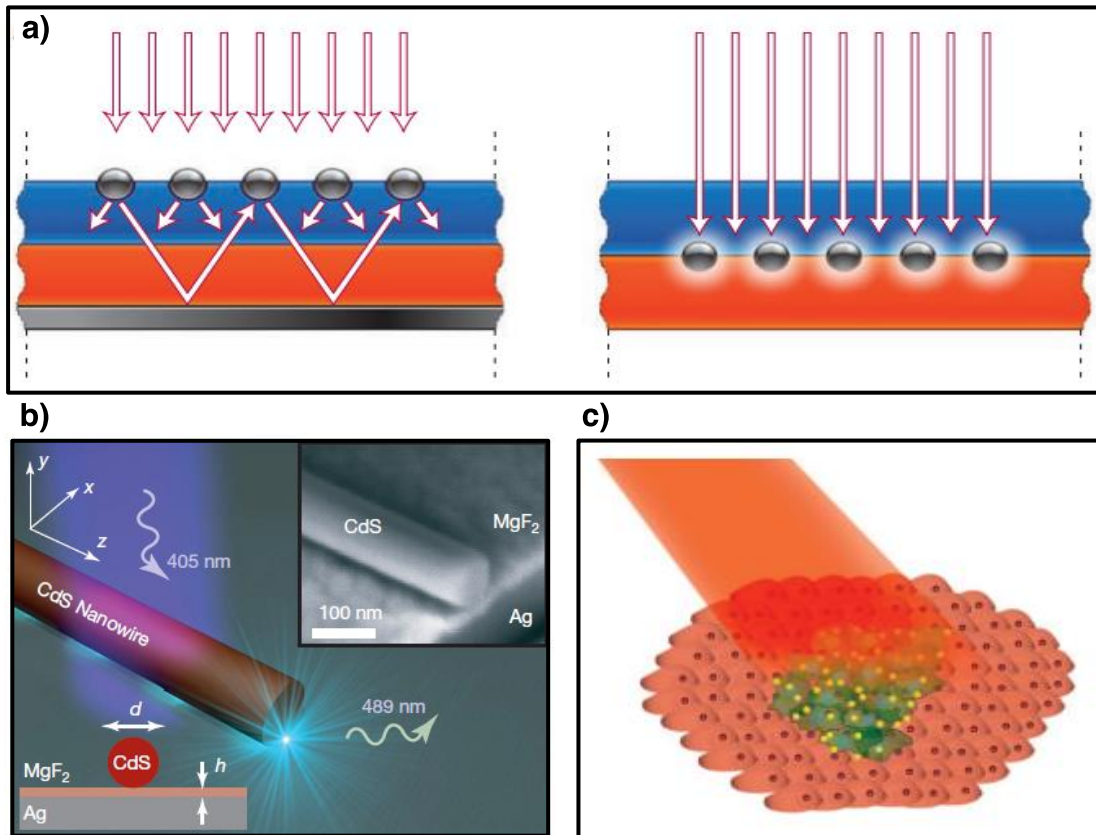


**Figure 2:** Application of plasmonic effects for (a) improved photovoltaic cells [14], (b) plasmonic lasers: SPASERS [17], and (c) photothermal therapies [16].

### 1.3 Plasmonic Polarization

Polarization dependence is a hallmark of plasmonic effect(s) occurring for device architecture(s). Plasmonic devices exhibit this polarization dependence with an increased response in optical emission.<sup>8,10,18</sup> Fig. 3 displays this polarization dependence for two types of device architecture and displays results for both transverse and longitudinal polarizations.<sup>8,19</sup>

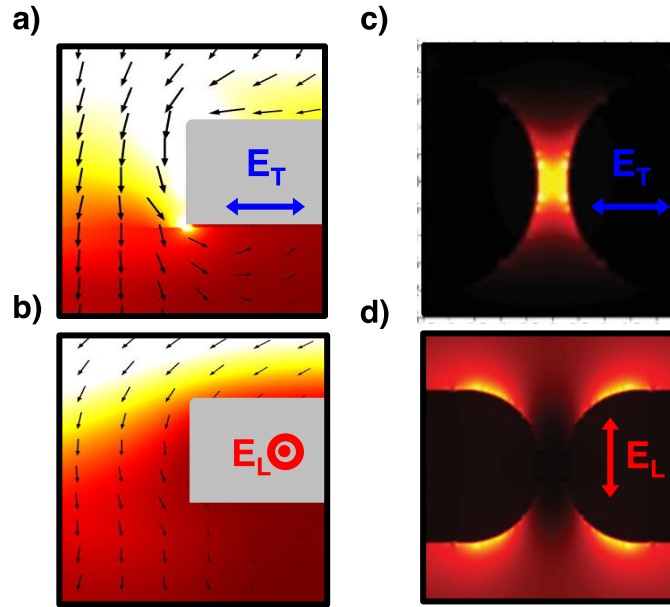


**Figure 3:** (a-b) Side-view and (c-d) Top-view results of computational electromagnetic modeling results showing plasmonic polarization dependence for both (a) and (c) transverse and (b) and (d) longitudinal polarizations. Plasmonic polarization dependence is shown for both (a-b) rectangular [8] and (c-d) circular shapes [19].

Both architectures in Fig. 3 have the longitudinal polarization traveling along the devices and the transverse polarization is traveling across the devices. The transverse polarization for both devices in Fig. 3 (a) and (c) show a greater device response in the computational results than the device response shown in (b) and (d). Both (c) and (d) show the top-side view of the nano-spheres and (a) and (b) show the side-view of the rectangular devices.

#### 1.4 Computational Electromagnetics

Computational electromagnetics (CEM) employs computer algorithms to provide solutions to complex electromagnetic problems; two popular methods in CEM are finite-difference time domain (FDTD) and finite-element method (FEM). The FDTD method employs a time domain to solve time dependent Maxwell's equations in partial differential equation form.<sup>20-22</sup> This study, however, will use FEM software (COMSOL Multiphysics), which employs a mathematical method to break the simulation space into a finite quantity of

mesh elements. This discretization of elements, shown in Figure 4, allows for these electromagnetic waves represented by complex differential equations to be expressed as basic functions.<sup>20</sup>

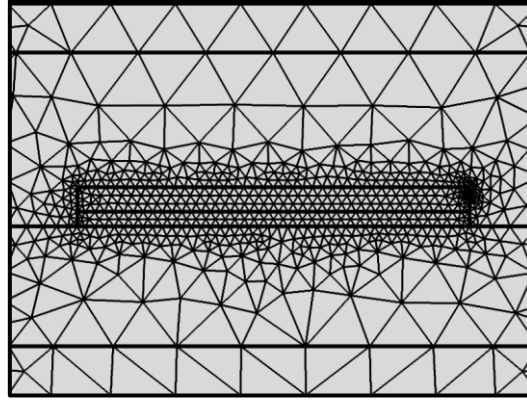


**Figure 4:** Finite Element Method (FEM) discretization of sample simulation space. Free triangular meshing pattern, simplifies complex partial differential equations that describe electromagnetic wave propagation into simple polynomials for each mesh element.

This component of FEM allows for very complex electromagnetic equations to be summarized in such a way that is not computationally intensive when compared to the number of elements that are created when finding a solution. Where the partial differential equation in the frequency domain for these models is given by

$$\nabla \times \mu_r^{-1}(\nabla \times \mathbf{E}) - k_0^2 \left( \epsilon_r - \frac{j\sigma}{\omega\epsilon_0} \right) \mathbf{E} = 0 \quad (1)$$

Where  $\nabla$  is the gradient function,  $\mu_r$  is the relative permeability of the material that the electromagnetic wave is propagating through,  $\mathbf{E}$  is the electric field,  $k_0$  is the initial wave number,  $\epsilon_r$  is the relative permittivity of the material that the electromagnetic wave is propagating through,  $j$  is the current density,  $\sigma$  is electrical conductivity of the material,  $\omega$  is the angular frequency, and  $\epsilon_0$  is the permittivity of free space. The electrical conductivity and the relative permittivity and permeability of the materials are defined within the COMSOL interface. The vector component of (1),  $\mathbf{E}$ , is given by

$$\mathbf{E}(x, y, z) = \mathbf{E}(x, z)e^{-ik_0y} \quad (2)$$

This expression shows that the electromagnetic waves conditions as modeled in a two-dimensional space can be polarized in the x and z directions and will propagate in the y direction. In addition to this meshing component, this simulation software treats a two-dimensional model as infinitely long along the device architecture as shown in Figure 5 (b). In addition to these models being treated as infinitely long in the z-direction, these particular models are created with periodic boundary conditions and perfectly matched layers. The model employed the radio frequency (RF) module of COMSOL to analyze these devices. This model is robust and has the capability to simulate variable physical parameters of the system in order to determine the enhancements properties of these devices. Variable input parameters include particular polarization, directional poynting vectors, material parameters, and geometry.

The wave equation to simulate these desired mechanics is  $E_{b,x} = e^{ik_0y}$ ; this equation represents the background electric field with a magnitude of 1 V/m that was incident on the structure for all simulations where a perfectly transverse polarization was employed. The equation components are as follows,  $i$  representing a complex number,  $k_0$  representing the initial wave number given by  $k_0 = \frac{2\pi}{\lambda}$ , and  $y$  is the k-vector direction, the direction in which light is propagating for this simulation. The initial wave number for the simulated models is a function of the wavelength of the incident light. This enables the modeled simulations to properly compute the electromagnetic response for the devices as a function of spectral input. For the longitudinal wave equation the background field would be  $E_L$ . In order to alternate between the two polarization angles, the background electric field equations were altered from the form given in (2) and the effect is shown by

$$E_{B,x} = e^{ik_0y} \cos(\theta) \quad (3)$$

$$E_{B,z} = e^{ik_0y} \sin(\theta) \quad (4)$$

Both (3) and (4) could be input into the initial physical conditions for all device designs and architectures and a incident polarization angle could be set so that the background electromagnetic conditions did not have to be changed from simulation to simulation. The electromagnetic response for a device is given by  $\Phi = \left| \frac{E_{local}^2}{E_0^2} \right|$  where  $\Phi$  is the optical enhancement characterized by the electromagnetic response of the device and  $E_{local}$  and  $E_0$  are the local and initial electric field respectively. The initial electric field is 1 V/m which reduces the equation for optical enhancement to  $\Phi = |E_{local}^2|$ .

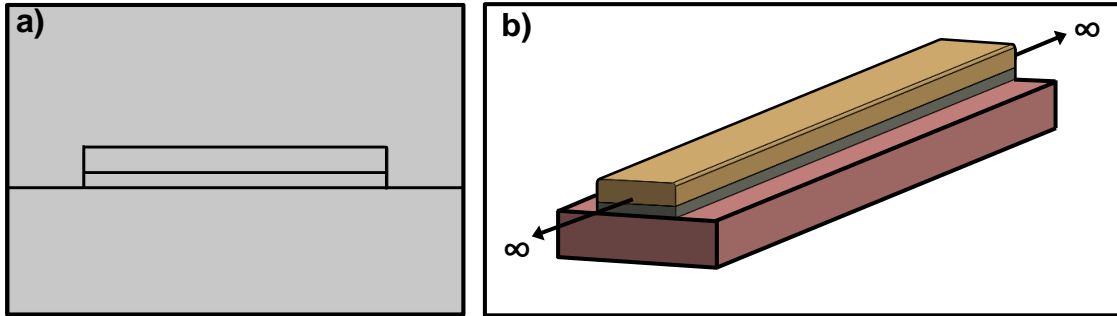


**Figure 5:** (a) Two dimensional rendering of sample structure, two-dimensional structures are treated as infinitely long in longitudinal direction, (b) Illustration of the two dimensional structure with infinitely long geometry in the z-direction (longitudinal).

When a device has been properly designed, meshed, all pertinent material properties entered, and electromagnetic conditions specified the software would display results similar to Figure 6.



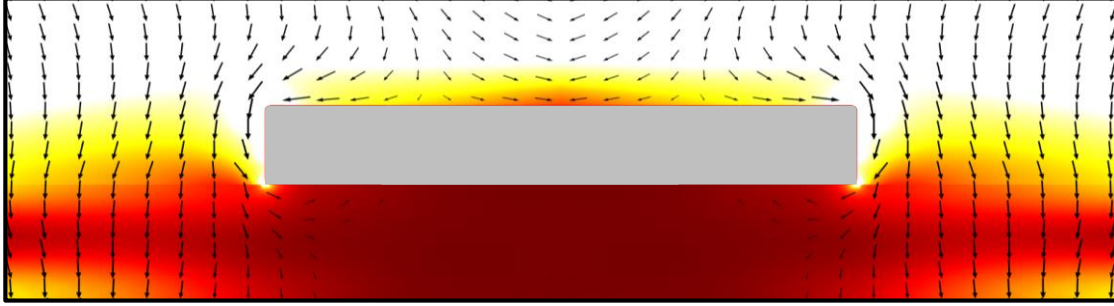


**Figure 6:** FEM result for sample structure shows optical enhancement distribution results for the sample structure and the direction of electromagnetic wave propagation and polarization.

The device structure will be displayed as well as the optical enhancement distribution for the particular physical situation created during the design of the simulation, optical enhancement for all device structures over a given area is given by

$$\Phi = \left| \sum \frac{E_{local}^2}{E_0^2} \right| = |\sum E_{local}^2| \quad (5)$$

Where  $E_{local}$  is the local electric field distribution and  $E_0$  is the initial electric field distribution, for the optical enhancement over a particular area, it is the sum each optical enhancement found for each mesh element. As the number of mesh elements increases, the size of the mesh elements decreases and the number of solutions computed for the local electric field as a result of the incident electromagnetic conditions increase. For this particular sample optical enhancement distribution, there is also an arrow map displaying the Poynting vector,  $\vec{S} = \vec{E} \times \vec{H}$  where  $\vec{E}$  is the electric field vector and  $\vec{H}$  is the magnetic field vector, for the electromagnetic wave with displayed transverse polarization. The Poynting vector describes the direction of electromagnetic wave due to the cross product between the electric and magnetic fields. The electromagnetic wave cannot fully penetrate the device material due to transmission losses, so the electromagnetic wave bends around the metallic layers. The distribution shown is a heat map with the white being the maximum value for the optical enhancement distributions and the black coloring being the minimum. From this type

of result, a more in-depth mathematical analysis can occur and other values can be derived from each particular result.

## **1.5 Thesis Motivation**

With the expansion of nanotechnology and the vastly improving computing power available currently, CEM has been explored in new and exciting mediums. Solutions to these complex electromagnetic problems are now available at the command of a few keystrokes, with the new level of computational ability, device optimization and creation is now more possible for device manufacture. CEM brings theoretical results that will help tune devices and systems for a wide array of applications as discussed in Section 1.2.

This work will analyze and further understand the potential plasmonic effects that could be occurring in an interdigital photodetector that is larger than customary devices that exhibit plasmonic activity; and to investigate the plasmonic enhancement that would occur if one were to fabricate these devices with geometrical specifications at the nanoscale.<sup>8,10</sup> Additionally, it will investigate new device architecture, Au thin-film microstructures. This particular device utilizes specific thin-film arrays and geometric dimensions of said microstructures to improve the photocurrent generation for electrodes.<sup>23</sup>

## Chapter 2: Interdigital Photodetectors

Note: Full details of this computational model and experimental results are found in submitted and published works [8] and [10] and contributed computational results to [26]. This chapter's results also presented in an invited presentation/talk at the INBRE conference in Fayetteville, AR in 2015.

### 2.1 Device Architecture and Simulation Setup

Semi-insulating GaAs photodetectors have been fabricated with interdigital gold electrode similar to the CdSe nanocrystal devices in previous work.<sup>9</sup> The electrode design of the devices is shown in Figure 7. They are gold electrodes with a titanium adhesion layer. Devices with various electrode widths,  $w$ , and electrode gap,  $g$ , were fabricated; and the ratio between the width of the electrode and the electrode gap was kept constant so that  $w = 2g$ , as the spacing increased for various device sizes.

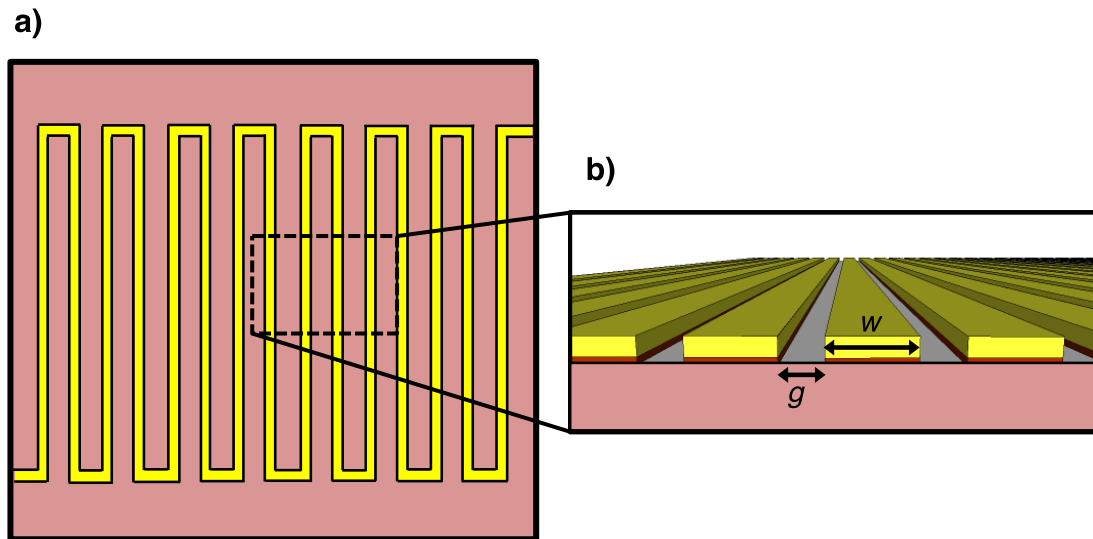


**Figure 7:** Microscopic views of the interdigital photodetectors of both (a) aerial, top-down and (b) cross-sectional slices of interdigital “fingers” with electrode width  $w$  and electrode gap  $g$ . [8, 10]

This device architecture shown in 7(b) was created in the COMSOL software to analyze the structure. This creation is shown in Figure 8.

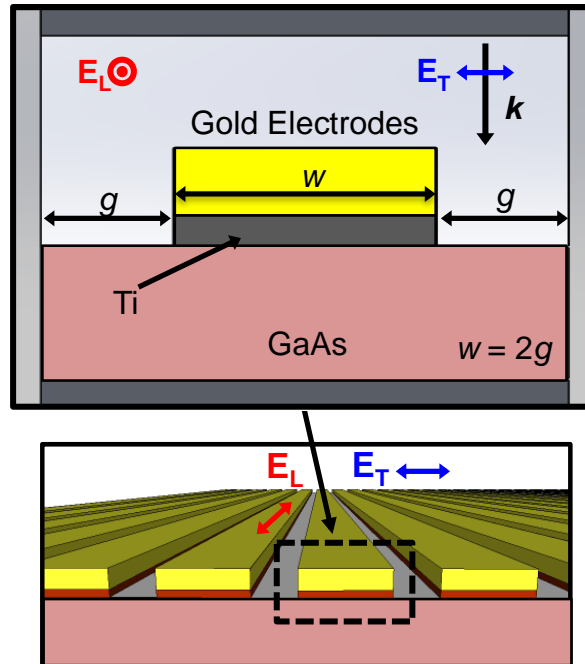


**Figure 8:** Simulation space creation for the interdigital photodetectors complete with: all material types (Au, Ti, GaAs), geometric conditions (electrode width and gap), electromagnetic wave polarization and poynting vector, periodic boundary conditions on the left and right boundaries, and perfectly matched layers on the top and bottom boundaries [8,10]

The simulation space as shown in Fig. 8 has periodic boundary conditions on the left and right sides of the simulation space. This was done so that the periodicity of the overall device could be maintained while the computational expense of the simulation run was minimized. As the overall simulation space increases the number of mesh elements needed to properly discretize the space also increases, which in turn drastically increases the number of solutions that have to be computed over the entire space. The particular material properties for this device were created using linear interpolation of experimental permeability and permittivity dielectric functions.<sup>24-25</sup> The top and bottom boundaries for the simulation space are perfectly matched layers; these boundaries prevent any electromagnetic waves from reflecting off of the material interface and causing interference in the simulation results. The perfectly matched layers encounter the electromagnetic waves and then scatter the waves to infinity, these perfectly matched layers are also referred to as perfectly absorbing

layers/boundaries. While the scattered to infinity or completely absorbing the electromagnetic waves are different effects, the result is the same, the simulated electromagnetic waves do not encounter the boundary and reflect back into the simulation causing interference.

## 2.2 FEM Analysis

The optical enhancement distribution for this particular device is shown in Figure 9.

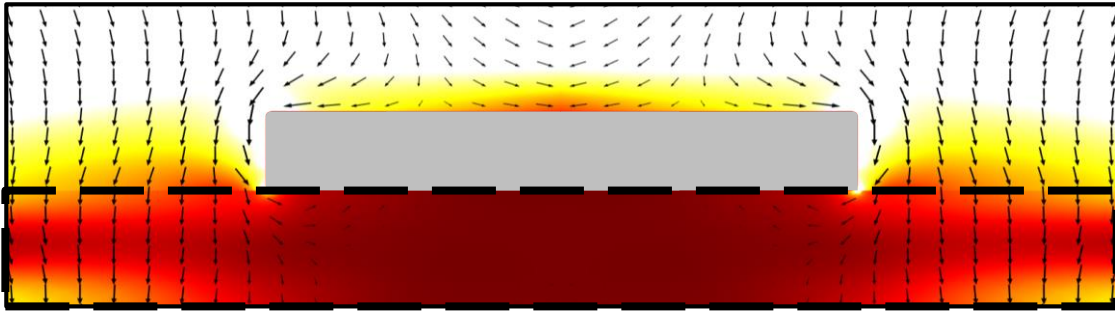


**Figure 9:** FEM result for structure shown in Figure 8 shows optical enhancement distribution results for the interdigital photodetector and the direction of electromagnetic wave propagation. Area encompassed by the dashed box is the GaAs substrate that is integrated over in order to determine the Optical Enhancement in the GaAs.

The area bounded by the dashed line in Fig. 9 was integrated over to find the summation of optical enhancement for all mesh elements for a wavelength of 875 nm. This summation is given in (1). The period of the device in Fig. 7 can be given as  $\Lambda = w + 2d$  and the cross-sectional area as  $A_{\Lambda} = a\Lambda$  where  $a$  is the height of the GaAs substrate in the simulation ( $a = 27 \mu m$  for this model). From these quantities, the photocarrier generation can be calculated by

$$G_0 = \frac{cn\varepsilon_0}{2h\nu A_{\Lambda}} \Phi \quad (6)$$

Where  $c$  is the speed of light,  $n$  is the refractive index of the GaAs substrate,  $\varepsilon_0$  is the permittivity of a vacuum,  $h$  is Planck's constant, and  $\nu$  is the frequency of the electromagnetic wave. From (6) the photocurrent generation can be calculated by

$$I_p = qwlG_0\tau(\mu_n + \mu_p)\frac{V}{g} \quad (7)$$

Where  $q$  is the charge of an electron,  $w$  is the width of the electrode,  $l$  is the total length of the electrode array under illumination,  $\tau$  is the decay time for the GaAs substrate,  $\mu_n$  and  $\mu_p$  are the mobility of the carries for the GaAs, and  $V$  is the applied bias voltage for experimentation. If you filter out the constant values in (7) a proportionality expression is developed that describes the variables that influence the photocurrent generation, this proportionality is given by

$$I_p \propto \frac{wl}{A\Delta g}\Phi \propto \frac{l}{g}\Phi \quad (8)$$

As shown in (8), the total length of the electrode that is illuminated by the incident light and the electrode gap are the two variables that most closely affect the photocurrent generation of the particular electrode architecture. It is important to understand what quantities affect the photocurrent generation the greatest so that devices can be created and tuned for particular applications/effects.

## 2.3 Electrode Gap Dependence

### 2.3.1 Micro-gaps

The electrode spacing dependence was investigated for the interdigital photodetectors for gap values of  $g = 5, 10, 20,$  and  $50 \mu m$  with the incident electromagnetic wave having transverse polarization,  $E_T$ . Experimental results were found for wavelengths in the visible spectrum to determine if there was a peak value for device response shown in Fig. 10(a).<sup>8,10</sup> The results found for both experimental response and calculated photocurrent generation for all electrode gaps for the peak wavelength found shown in Fig 10(b) and (c).<sup>8</sup>

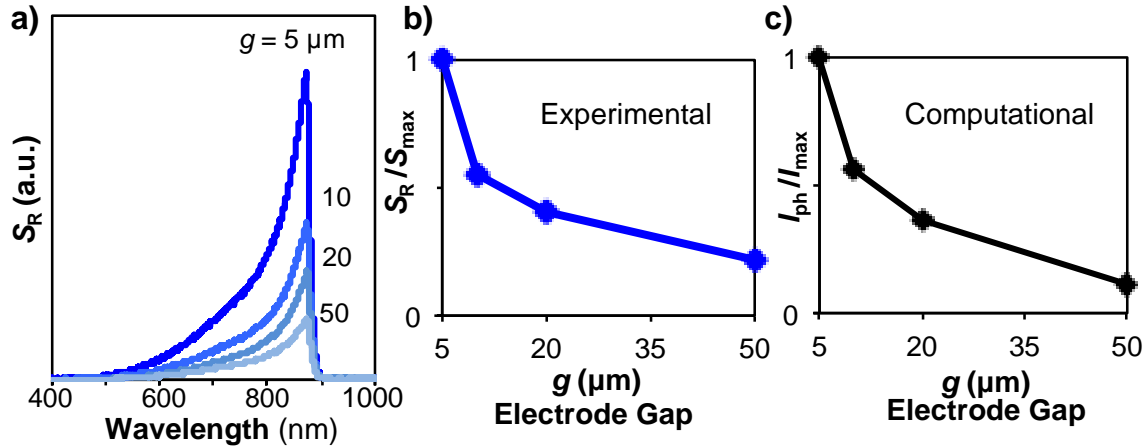


**Figure 10:** Electrode gap experimental results of interdigital photodetectors shown in Figure 7 showing (a) band gap of GaAs at 875 nm and increase in spectral response as electrode gap is reduced and (b) normalized spectral response at 875 nm wavelength band gap of GaAs. (c) Normalized computational results of the interdigital photodetectors simulation space shown in Figure 8. [8,10]

As shown, 10 (b) and (c) are the normalized results for both the experimental and computational results, respectively. Both graphs match very well and display the same trend that as the electrode gap decreases the device response increases. These results were similar to a previous work that was completed for another member of the research group.<sup>26</sup> That particular work focused on the effect of a shrinking nanogap and the effect that the smaller nanogap had on the maximum optical enhancement found in said nanogap. This trend is shown in Figure 11.

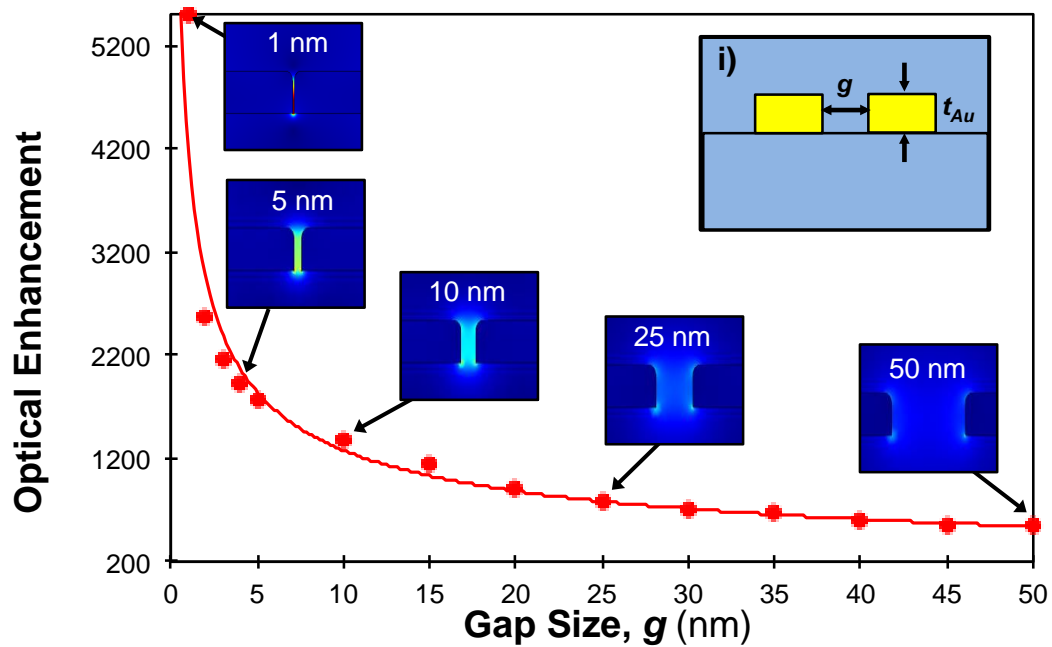


**Figure 11:** Optical enhancements of Au nanostructure shown in (i) with gap spacing,  $g$ , variable from 1 nm to 50 nm. (i) Au Nanostructure with constant  $t_{Au}$  and variable gap spacing  $g$ . [26]

The device architecture is shown in 11(i) where nanostructure gap  $g$  was variable and the thickness of the Au slab was kept constant. Within the graph, there are electric field distribution images for gaps of  $g = 1, 5, 10, 25,$  and  $50$  nm. The color map for these images has a deep red color for most intense and deep blue for least intense. As the nanostructure gap is reduced the optical enhancement exhibited by the device increases. Traditional plasmonic effects are most prevalent at the nanoscale due to the lifespan of the actual oscillating plasmon. The similarity in trends is a major indicator that the effects being seen in the interdigital photodetectors is plasmonic in spite of its geometric size even if those effects at the microscale are small relative to nanoscale effects. Additionally, the microscale interdigital photodetectors display similar plasmonic hotspots at the edges of the device that are shown in the electric field distributions of the nanostructures shown in Fig. 11.



### 2.3.1 Nano-gaps

Presently only microscale photodetectors have been fabricated. This work also examined nanostructure models for potential nanofabrication of similar structures. Much of this was to understand what would occur with the device at this scale and determine how the material components, geometrical ratios, and intrinsic properties of the materials would be affected when the device scaled to nanometers. The simulation space was created in the same fashion as previously described for the microscale devices, however, for this nanogap architecture, the gap size went as low as  $g = 25$  nm. Figure 12 shows the optical enhancement for the nanoscale device<sup>10</sup>.

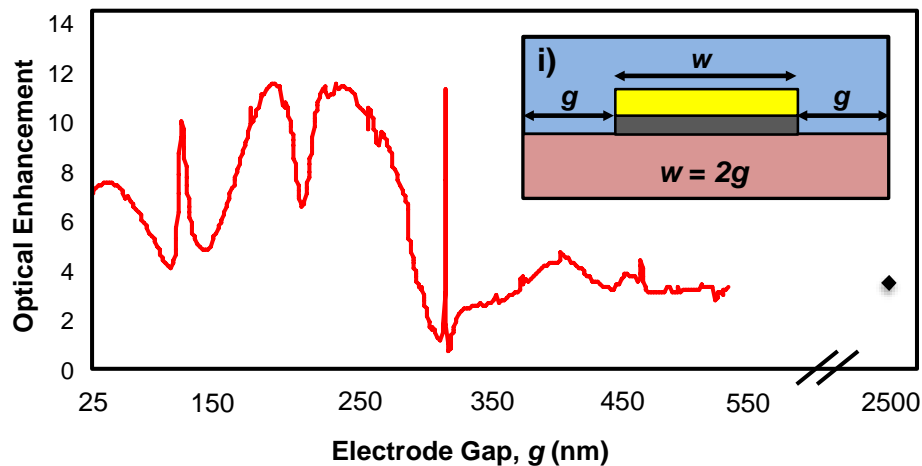


**Figure 12:** Optical enhancement of interdigital photodetector configuration shown in (i). Optical enhancement is a function of electrode gap, which impacts the electrode width, and periodicity of the device architecture [10].

The device architecture is shown in 12(i) where the key geometric ratio of  $w = 2g$  is kept constant even when the overall device size is reduced down to the nanometer range. The far right black diamond on the graph is the  $5 \mu m$  point that was the maximum optical enhancement value found in the computational microscale study. When the electrode gap  $g$  is increased to 400 nm, the optical enhancement found in the GaAs substrate is found to be approximately constant at a value of  $\sim 3.8$  even as the electrode gap increases to the  $5 \mu m$

point. The overall trend of the optical enhancement for the nanoscale device heavily depends on the periodicity of the device. Where the period is  $\Lambda = w + 2g = 3g$ . Plasmonic gratings have been shown to increase optical enhancement of the device as a means to improve plasmonic applications.<sup>27-29</sup>

## 2.4 Polarization Dependence

Polarization dependent measurements were taken to investigate the role of plasmonic effects enhancing the response of the device. The spectral response measurements were performed for an electrode gap of  $g = 5\mu m$ . Figure 13(a) displays these results with transverse  $E_T$  and longitudinal  $E_L$  polarizations.<sup>8,10</sup> When the polarization was across the device structure,  $E_T$  the device exhibited a larger spectral response; however, when the polarization was rotated  $90^\circ$  to propagating longitudinally,  $E_L$ , the spectral response was greatly reduced. Fig. 13(b) shows experimental polarization results in green squares and the calculated photocurrent found by the computational simulations in the blue circles. The experimental values were found using a similar setup and the inclusion of a linear polarizer; the full setup is described here<sup>8</sup>. A perfectly transverse incident polarization angle is given as  $0^\circ$  and a perfectly longitudinal incident polarization angle is given as  $90^\circ$ .

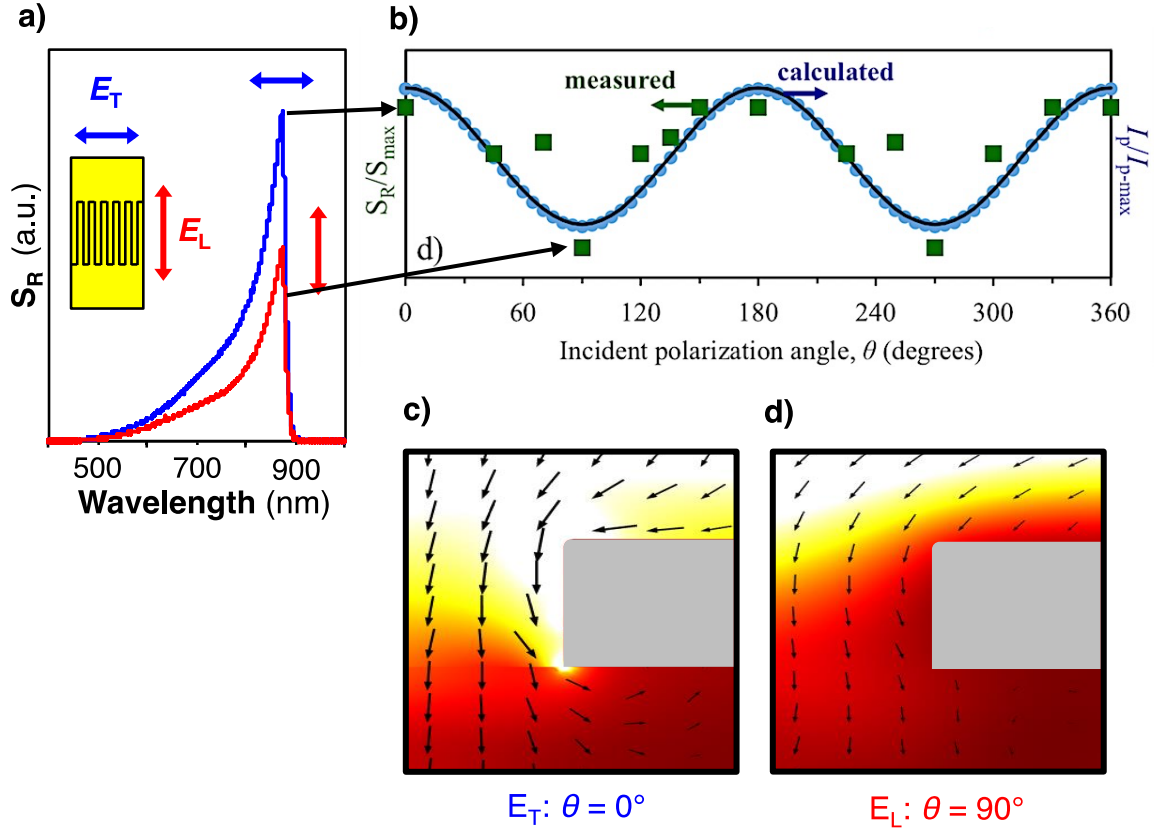


**Figure 13:** (a) and (b) Polarization study of the interdigital photodetectors with electrode gap  $5 \mu m$  showing (a) spectral study of the photodetector with peak response at  $875 \text{ nm}$  wavelength and (b) measured spectral response shown by the green squares and calculated photocurrent generation by the computation electromagnetic studies shown by the blue circles; both measured SR and calculated IP are shown for different incident electromagnetic wave polarizations. [8, 10]

This result in 13(a) shows a significant dependence on electromagnetic polarization for device response. This polarization dependence was investigated for polarizations outside of perfectly transverse or longitudinal. Fig.13 (b) shows the measured spectral responses in green squares for a variety of incident polarization angles for a device with electrode gap  $g = 5 \mu m$ . Because of the displayed experimental polarization dependence, the device was investigated by modeling a  $g = 5 \mu m$  electrode gap and varying the incident polarization angle,  $\theta$ , between transverse and longitudinal polarizations every  $5^\circ$  to find the optical enhancements and then the photocurrent generation from the process outline in Section 2.2. Fig. 13(c) and (d) show the optical enhancement distributions for both perfectly (c)  $E_T$  and

(d)  $E_L$  polarizations, 13(c) shows that more light is scattered into the GaAs substrate than the longitudinal polarization shown in 13(d). This is likely due to surface plasmonic effects at the edges of the Au electrode and the exhibited polarization dependence shown in Fig. 13 is similar to the dependence shown in other plasmonic devices.<sup>6,30-33</sup> The calculated photocurrent generation results in Fig. 13(b) match well with the experimental results in Fig. 13(a), with the ratio between longitudinal and transverse spectral response being defined by  $r_S = \frac{S_T}{S_L} = 1.7$  and the ratio between longitudinal and transverse photocurrent generation being defined by  $r_I = \frac{I_T}{I_L} = 1.5$ .

## Chapter 3: Au Thin-Film Microstructure

Note: This chapter is currently in preparation for publication: [23].

### 3.1 Device Architecture and Simulation Setup

The device is comprised of arrays of thin-film microstructures deposited on a semi-insulating GaAs substrate with a titanium adhesion layer to bond the topmost gold layer to the GaAs substrate.<sup>23</sup> The necessity of the titanium adhesion layer was also investigated to determine the viability of the photodetectors without such a layer and the impact that the adhesion layer would have on the spectral response and optical enhancement. The arrays are  $20\ \mu\text{m} \times 20\ \mu\text{m}$  slabs spaced by  $100\ \mu\text{m}$  longitudinally and  $40\ \mu\text{m}$  transversely. This device is shown in schematic form in Figure 14.

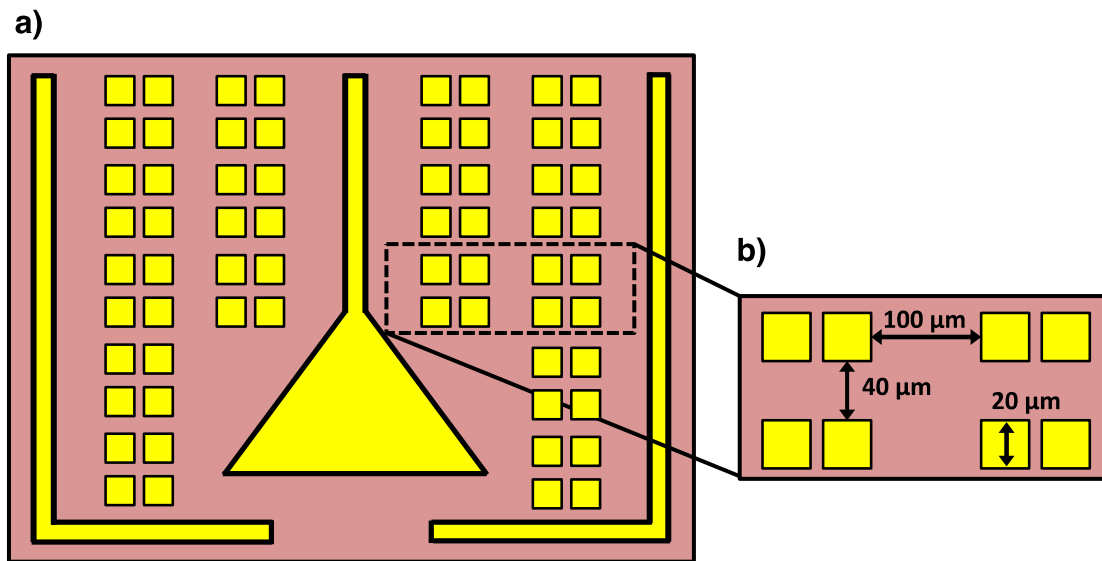


**Figure 14:** Microscopic views of Au thin-film microstructures device of both (a) aerial, top-down and (b) linear array structures with  $100\ \mu\text{m}$  transverse separation,  $40\ \mu\text{m}$  longitudinal separation, and  $20\ \mu\text{m}$  structure length [23].

The photodetector was created such that three planar gold electrodes were deposited on the GaAs substrate and the central-most electrode was created with a triangle base in order for more effective wire bonding. The process by which the device was created is detailed here.<sup>23</sup> The thin-film microstructure architecture was created in the computational

software in a similar process that was described earlier in Chapter 2. The simulation space design is shown schematically in Figure 15.

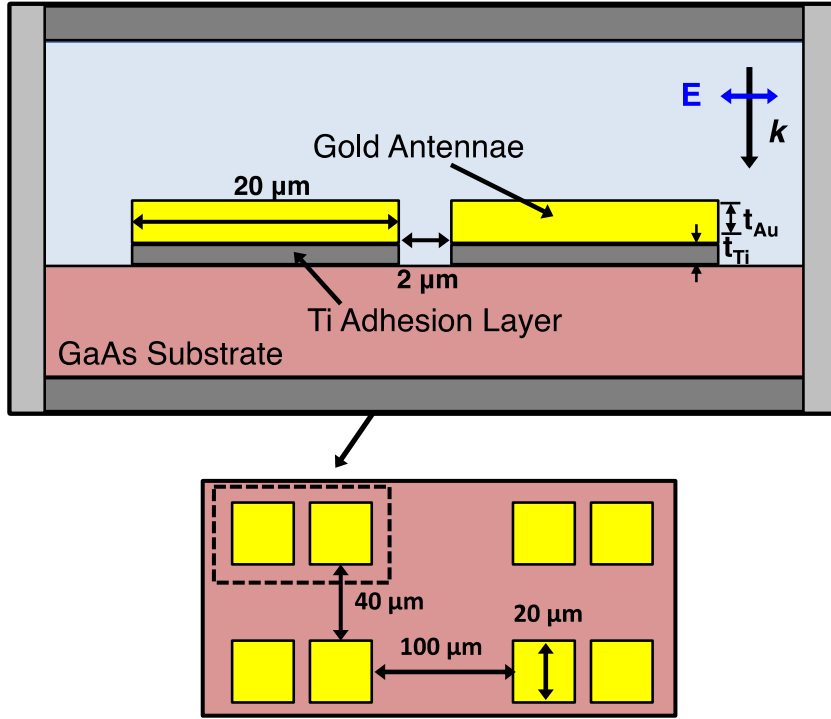


**Figure 15:** Simulation space creation for the thin-film microstructure device complete with: all material types (Au, Ti, GaAs), geometric conditions (slab width and spacing and Au and Ti thicknesses), electromagnetic wave polarization and poynting vector, periodic boundary conditions on the left and right boundaries, and perfectly matched layers on the top and bottom boundaries [23].

Both the Au slab and Ti adhesion layers are  $20 \mu m$  in width with  $2 \mu m$  slab separation that is held constant for this device. The thickness of both the Au slab,  $t_{Au}$ , and Ti adhesion layer,  $t_{Ti}$ , were investigated for improvement factors in photocurrent generation and optical enhancement. Similarly to the interdigital photodetectors described in Chapter 2, the left and right boundaries for this simulation are periodic boundary conditions to model the array structure that defines the device and the top and bottom boundaries are permanently matched layers that prevent any reflect electromagnetic waves from causing interference in the simulation. Polarization dependence was not investigated for this device, only transverse,  $E_T$ , polarization was investigated with a downward poynting vector as shown in Fig. 15. Au

heights of  $t_{Au} = 10, 20, 30, 40, 50 \text{ nm}$  and Ti adhesion layer heights of  $t_{Ti} = 0, 1, 2, 3, 4 \text{ nm}$  were investigated for this study.

### 3.2 Experimental Photocurrent Generation and Calculated Optical Enhancement

The experimental photocurrent generation was measured and the methods are described in this work.<sup>23</sup> The effects of altering both the Au and Ti thickness is characterized in Figure 16, showing both experimental improvement with the introduction of the thin-film microstructure in photocurrent generation and the theoretical optical enhancement exhibited by the device.

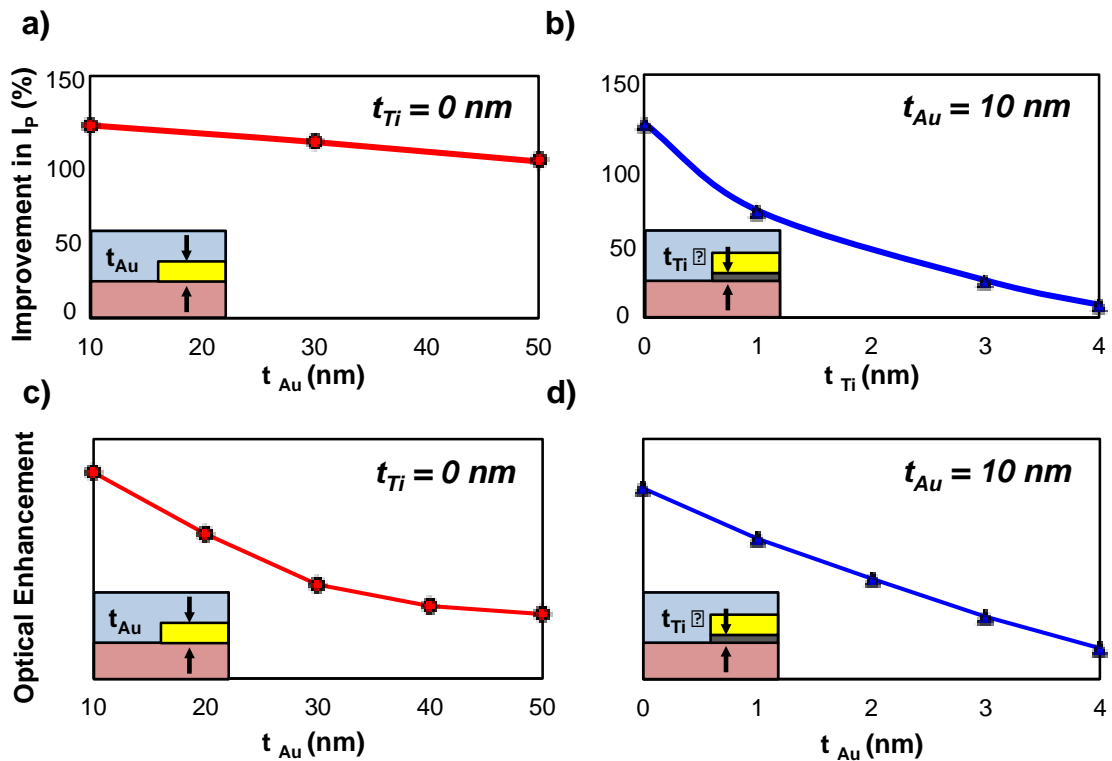


**Figure 16:** (a) and (b) experimental results showing improvement in photocurrent generation of microstructure devices for (a) no Ti adhesion layer and variable Au thickness and (b) constant 10 nm Au thickness and variable Ti thickness. (c) and (d) computation results showing optical enhancement measured in the GaAs substrate for (c) no Ti adhesion layer and variable Au thickness and (d) constant 10 nm Au thickness and variable Ti thickness. [23]

Fig. 16 (a) and (c) show the improvement in photocurrent generation and optical enhancement, respectively, for a variable Au microstructure thicknesses only, with no Ti

adhesion layer. Fig 16 (b) and (d) show the improvement in photocurrent generation and optical enhancement, respectively, for a variable Ti adhesion thickness with a constant Au thickness of 10 nm. The improvement in the photocurrent generation is given by

$$\text{Improvement } I_p = \frac{I_{P,with} - I_{P,without}}{I_{P,without}} \quad (9)$$

As shown in Fig. 16, the overall results match relatively well, with both geometric constraints providing similar trends in device response. As the thickness of both the Au microstructure and Ti adhesion layer increases the response of the device decreases. This is not an entirely accurate portrayal of the actual response of the device though, the experimental measurements as shown describe an improvement in the photocurrent generation as compared to no Au microstructure or Ti adhesion layer being present in the electrode schematic; whereas, the computational results only show the optical enhancement for each respective  $t_{Au}$  and  $t_{Ti}$  variable.

### 3.3 Improvement Factors

In order to properly characterize the actual computational results for the introduction of the microstructure, improvement factors for both the experimental photocurrent generation and the theoretical optical enhancements had to be found and compared against one another. The improvement factor for the optical enhancement can be characterized by

$$\text{Improvement } \Phi = \frac{\Phi_{with} - \Phi_{without}}{\Phi_{without}} \quad (10)$$

Where the improvement is characterized as the percent increase in response of the device with and without the microstructures. This improvement is shown for both experimental photocurrent generation and theoretical optical enhancement in Figure 17.



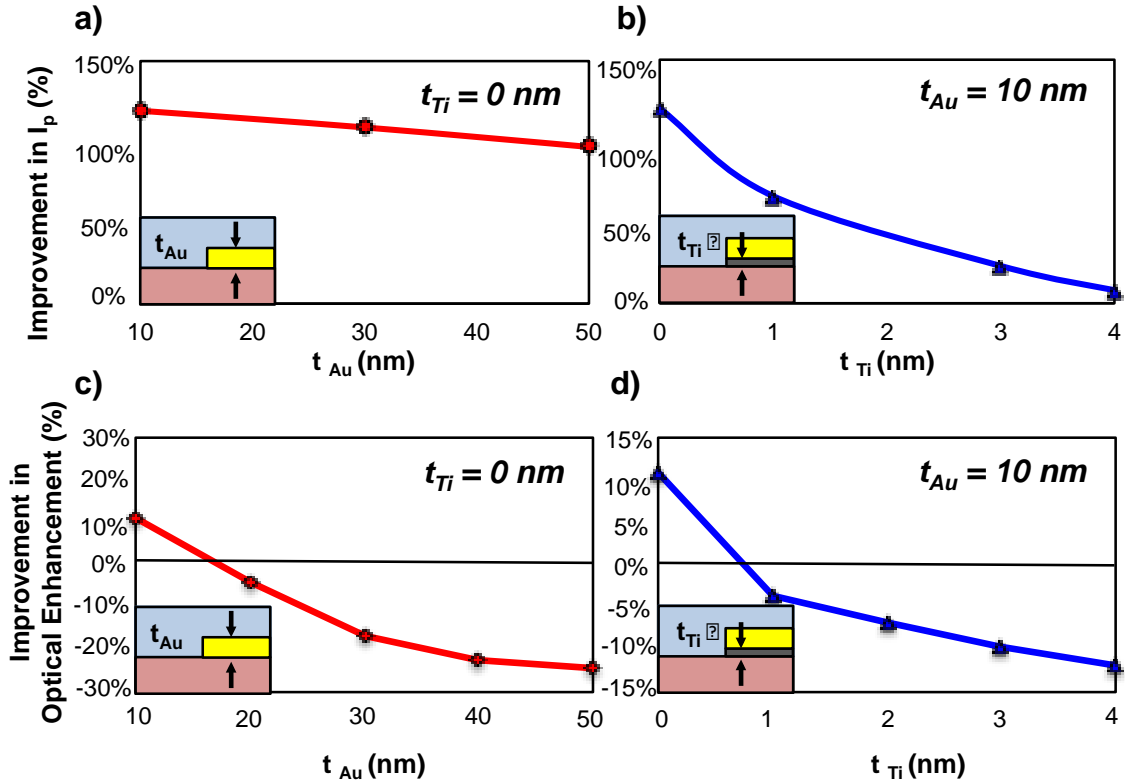


**Figure 17:** Improvement in (a) and (b) spectral response and in (c) and (d) optical enhancement. Where (a) and (c) have no Ti adhesion layer and variable Au thickness and (b) and (d) have constant 10 nm Au thickness and variable Ti thickness. Computation results in (c) and (d) showing improvement in optical enhancement as negative is indicative of no plasmonic improvement from the introduction of the microstructure in the device architecture. [23]

The improvement found in the optical enhancement show that there should not be any improvement in device response that can be attributed to plasmonic effects. As described in Chapter 1, these models were created using the RF module in COMSOL to simulate electromagnetic wave effects for the simulations and because the results in Fig. 17 (c) and (d) show a decrease in performance, it cannot be said that these microslab devices are improved because of plasmonic effects. The improvement that is shown in the photocurrent generation is most likely due to the excitation of hot electrons.<sup>23</sup>

### 3.4 FEM Optical Enhancement Distribution

Though plasmonic effects cannot characterize the improvement in device response, there does appear to be plasmonic activity occurring with the microstructure architecture.

The optical enhancement decreasing as Au and Ti thickness increases shown in Fig. 16 (c) and (d) is similar to other work.<sup>29</sup> Figure 18 shows the optical enhancement distributions for Au thickness of  $t_{Au} = 10, 30,$  and  $50$  nm and Ti thickness of  $t_{Ti} = 0, 1,$  and  $4$  nm.

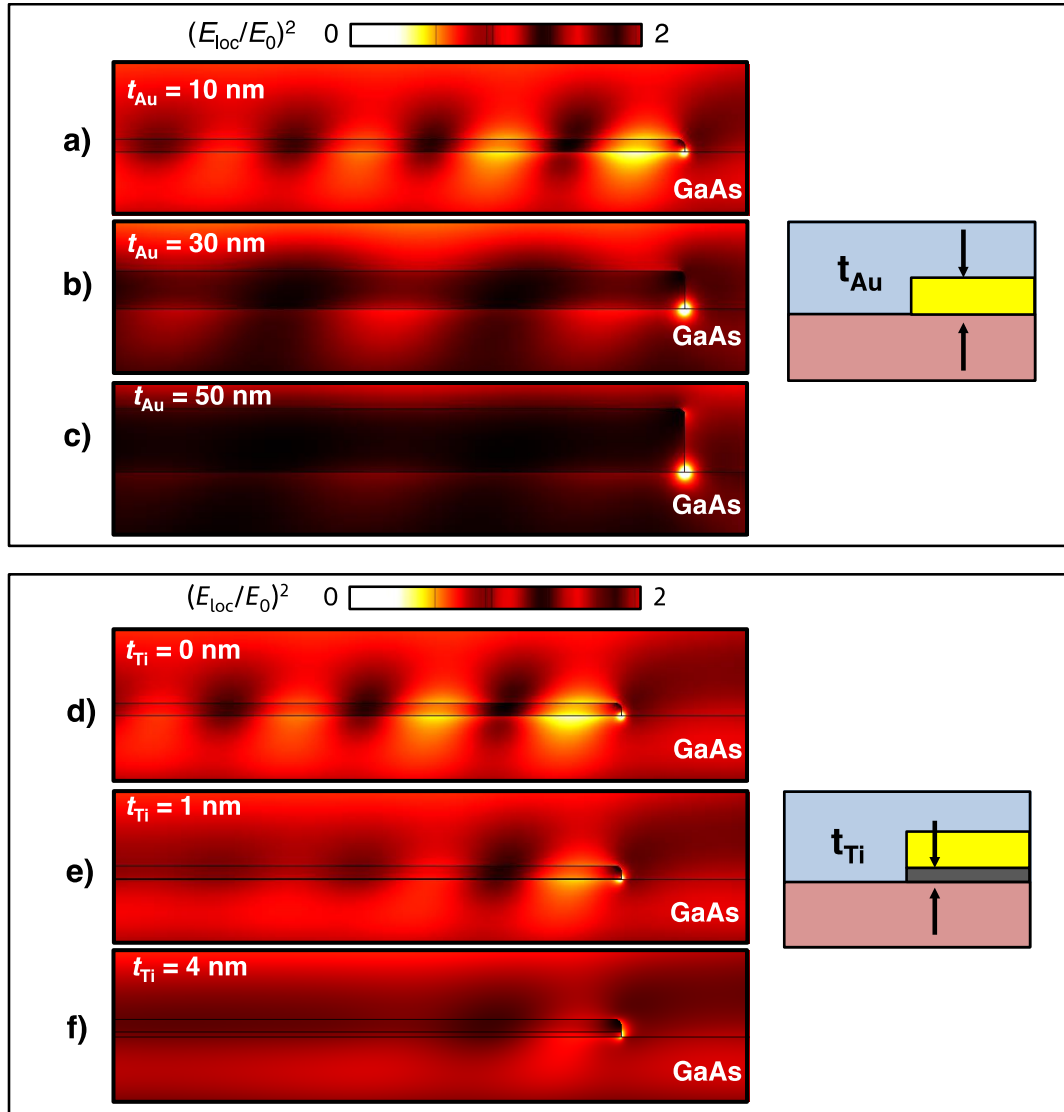


**Figure 18:** Optical enhancement distributions for Au thin-film microstructure devices (a), (b), and (c) variable Au thicknesses and no Ti adhesion layer and for (d), (e), and (f) variable Ti thickness and a constant 10 nm Au thickness. [23]

Fig. 18 (a)-(c) pictorially show the Au thickness variants and the device architecture is shown as well. As the thickness of the Au slab increases, the overall optical enhancement of the device decreases, graphically shown in Fig. 16(c). Fig 18 (d)-(f) shows the Ti thickness

variants and the device architecture, for this simulation, the Au thickness was held fixed at  $t_{Au} = 10$  nm. As the thickness of the Ti increases the overall optical enhancement of the device decreases, graphically shown in Fig. 16 (d). Shown in the optical enhancement distributions in Fig. 18 (a)-(f) there is a localized plasmonic hotspot at the edge of the Au/Ti layers at the interface between the metallic structure and the GaAs substrate. Also shown is an oscillation in the intensity of the optical enhancement for both the Au and Ti variants in Fig. 18 (a)-(f); this oscillation in intensity is the greatest when the thicknesses for both the Au and Ti are minimized. It is thought that these oscillations in intensity are pictorially manifested plasmonic wave oscillations. As the thickness is reduced for both Au and Ti, the wavelength of the plasmonic wave increases until it reaches its maximum and the wave is damped out when the thicknesses are increased. More work needs to be done to further analyze and understand exactly what is occurring with this plasmonic wave oscillation.

## Chapter 4: Conclusion

This work focused on investigating the potential plasmonic activity occurring in microelectronic and photonic devices and determining if those plasmonic effects were still present or even improved at the nanoscale. For the interdigital photodetectors, it was determined that the devices do exhibit plasmonic effects both in the optical enhancement increase as the electrode gap decreased and also by the polarization dependence of the devices. In order to determine the relationship between the experimental results and the theoretical models, an equation describing the correlation between the optical enhancement and the photocurrent generation. It was determined that the two variables that most closely affect the photocurrent generation of the interdigital photodetectors are the overall length of the electrodes exposed to incident illumination and the electrode gap of the electrode. It was also determined that when the device architecture of the interdigital photodetectors is reduced to the nanoscale the plasmonic effects are still in effect, but the periodicity of the overall structure because integral to the plasmonic performance of the device. The investigation of the interdigital photodetectors at the nanoscale only focused on the transverse polarization and variable incident polarization angle should be examined in future works.

This work also investigated a new type of electrode device, one that utilized potential plasmonic effects to enhance the photocurrent generation of the electrodes with the introduction of microslabs into the device architecture. It was determined that the Au thin-film microstructures caused both an increase in measured photocurrent generation and an increase in the theoretical optical enhancement simulated. However, when compared to the introduction of the microslabs versus the electrodes without the microstructures, the theoretical improvement in optical enhancement did not actually prove to be plasmonically

related. Experimentally, it was found that the photocurrent generation was greatly improved by the introduction of the microstructures; however, that was not the case for the optical enhancement found in the modeled simulations. This leads to the conclusion that the improvements by the introduction of the microstructures is not actually due to plasmonic effects but rather, it is caused by hot electron effects.

Computational modeling allows for complex geometrical, material, and physical properties to be simulated and examined with greater precision than previously allowed. These simulations provide vast amounts of information to better fabricate and design these photodetector devices, and through simulation work, the devices can be tuned to specific applications and desired optical enhancements.

## Bibliography

1. J. B. Pendry, A. J. (1996). Extremely Low Frequency Plasmons in Metallic Mesostructures. *Physics Review Letters* , 76 (25), 4773-4776
2. Dmitri K. Gramotnev, S. I. (2010). Plasmonics beyond the diffraction limit. *Nature Photonics* , 83-91.
3. Nature Nanotechnology. (2015). Nano-optics gets practical. *Nature Nanotechnology* , 10 (1), 11-15.
4. Maier, S. (2007). *Plasmonics: Fundamentals and Applications*. Boston, MA, USA: Spring USA.
5. Douglas Natelson, Y. L. (2013). Nanogap structures: combining enhanced Raman spectroscopy and electronic transport. *Physical Chemistry Chemical Physics* , 15 (15), 5262.
6. J. B. Herzog, M. W. (2013). Dark Plasmons in Hot Spot Generation and Polarization in Interelectrode Nanoscale Junctions. *Nano Letters* , 13 (3), 1359-1364.
7. Yaking Li, J. B. (2013). Nanogap structures: combining enhanced Raman spectroscopy and electronic transport. *Physical Chemistry Chemical Physics* , 15 (15), 5262.
8. A. I. Nusir, **A. M. Hill** (2015). Near-infrared metal-semiconductor-metal photodetector based on semi-insulating GaAs and interdigital electrodes. *Photonics Research* , 3 (1), 1.
9. A. I. Nusir, J. A. (2014). Uncooled Photodetectors based on CdSe nanocrystals with an interdigital metallization. *Applied Physics Letters* , 104 (5), 051124.
10. **A. M. Hill**, A. I. (2014). Computation electromagnetic analysis of plasmonic effects in interdigital photodetectors. *9163*. SPIE.
11. Oliveros R. Rodriguez, J. A.-G. (2012). Gold Nanostars as thermoplasmonic nanoparticles for optical heating. *Optics Express* , 20 (1), 621.
12. Joseph B. Herzog, M. W. (2014). Thermoplasmonics: Quantifying Plasmonic Heating in Single Nanowire. *Nano Letters* , 14 (2), 499-503.
13. Y. Jiao, L. H. (2013). Widening Absorption Band of Grating Structure With Complex Dual-Groove Grating. *Journal of Heat Transfer* , 135 (3), 032701-032701.
14. Harry A. Atwater, A. P. (2010). Plasmonics for improved photovoltaic devices. *Nature Materials* , 205-213.

15. E. T. Yu, D. D. (2008). Plasmonic nanoparticle scattering for enhanced performance of photovoltaic and photodetector devices. *7033. SPIE.*
16. Surbgi Lal, S. E. (2008). Nanoshell-Enabled Photothermal Cancer Therapy: Impending Clinical Impact. *Accounts of Chemical Research* , 41 (12), 1842-1851.
17. Rupert F. Oulton, V. J.-M. (2009). Plasmon lasers at deep subwavelength scale. *Nature* , 461 (7264), 629-632.
18. Hua Qi, R. W. (2012). Polarization Dependence of Surface Enhanced Raman Scattering on a Single Dielectric Nanowire. *Journal of Nanomaterials* , e946868.
19. A. Garcia-Martin, D. R. (2011). Field Enhancement in subnanometer metallic gaps. *Physical Review B* , 83 (19), 193404.
20. E. Vandenbosch, G. A. (2012). Computational Electromagnetics in Plasmonics. In *Plasmonics - Principles and Applications*. InTech.
21. Alexander Axelevitch, B. A. (2013). Simulation and experimental investigation of optical transparency in gold island films. *Optics Express* , 21 (4), 4126.
22. Alexei Deinega, S. B. (2009). Hybrid transfer-matrix FDTD method for layered periodic structures. *Optics Letters* , 34 (6), 860-862.
23. A. I. Nusir, **A. M. Hill** (2016). Generation of Hot Electrons in microscale Au thin-film to enhance near-infrared photodetection, (in preparation).
24. P. B. Johnson, R. W. (1972). Optical Constants of the Noble Metals. *Physical Review B* , 6 (12), 4370-4379.
25. Y. Todorov, L. T. (2010). Optical properties of metal-dielectric-metal microcavities in the THz-frequency range. *Optics Express* , 18 (13), 13886-13907.
26. Stephen J. Bauman, D. T. Debu, **Avery M. Hill** (2015). Plasmonic structures fabricated via nanomasking sub-10 nm lithography technique. *9556. SPIE.*
27. Stephen Bauman (2015). Fabrication of Sub-Lithography-Limited Structures via Nanomasking Technique for Plasmonic Enhancement Applications. *IEEE Transactions on Nanotechnology* , 14 (5), 790-793
28. Ahmad A. Darweesh, Stephen J. Bauman (2016). Optical Enhancement in double-width plasmonic gratings with sub-10 nm nanogaps fabricated with blanket nanomasking technique. *Optical Society of America*, Submitted 2016
29. Cameron Saylor, Eric Novak (2015). Investigation of maximum optical enhancement in single gold nanowires and triple nanowire arrays. *Journal of Nanophotonics*, 9 (1), 093053.

30. H. Chalabi, D. S. (2014). Hot-electron photodetection with a plasmonic nanostripe antenna. *Nano Letters* , 14, 1374-1380.
31. J. Hetterich, G. B. (2007). Optimized design of plasmonic MSM photodetector. *IEEE J. Quantum Electron* , 43, 855-859.
32. F. Ren, K. W. (2010). Surface plasmon enhanced responsivity in a waveguided germanium metal-semiconductor-metal photodetector. *Applied Physics Letters* , 97, 091102.
33. B.Y. Zheng, Y. W. (2014). Color-selective and CMOS-compatible photodetection based on aluminum plasmonics. *Advanced Materials*, 26, 6318-63.